

Ultrafast photocurrents at the surface of the three-dimensional topological insulator Bi 2 Se 3

Lukas Braun, Gregor Mussler, Andrzej Hruban, Marcin Konczykowski,
Thomas Schumann, Martin Wolf, Markus Münzenberg, Luca Perfetti, Tobias
Kampfrath

► **To cite this version:**

Lukas Braun, Gregor Mussler, Andrzej Hruban, Marcin Konczykowski, Thomas Schumann, et al.. Ultrafast photocurrents at the surface of the three-dimensional topological insulator Bi 2 Se 3. Nature Communications, Nature Publishing Group, 2016, 7, pp.13259. 10.1038/ncomms13259 . hal-01445495

HAL Id: hal-01445495

<https://hal-polytechnique.archives-ouvertes.fr/hal-01445495>

Submitted on 24 Jan 2017

HAL is a multi-disciplinary open access archive for the deposit and dissemination of scientific research documents, whether they are published or not. The documents may come from teaching and research institutions in France or abroad, or from public or private research centers.

L'archive ouverte pluridisciplinaire **HAL**, est destinée au dépôt et à la diffusion de documents scientifiques de niveau recherche, publiés ou non, émanant des établissements d'enseignement et de recherche français ou étrangers, des laboratoires publics ou privés.

ARTICLE

Received 10 Nov 2015 | Accepted 16 Sep 2016 | Published 31 Oct 2016

DOI: 10.1038/ncomms13259

OPEN

Ultrafast photocurrents at the surface of the three-dimensional topological insulator Bi_2Se_3

Lukas Braun¹, Gregor Mussler², Andrzej Hruban³, Marcin Konczykowski⁴, Thomas Schumann⁵, Martin Wolf¹, Markus Münzenberg⁵, Luca Perfetti⁴ & Tobias Kampfrath¹

Three-dimensional topological insulators are fascinating materials with insulating bulk yet metallic surfaces that host highly mobile charge carriers with locked spin and momentum. Remarkably, surface currents with tunable direction and magnitude can be launched with tailored light beams. To better understand the underlying mechanisms, the current dynamics need to be resolved on the timescale of elementary scattering events (~ 10 fs). Here, we excite and measure photocurrents in the model topological insulator Bi_2Se_3 with a time resolution of 20 fs by sampling the concomitantly emitted broadband terahertz (THz) electromagnetic field from 0.3 to 40 THz. Strikingly, the surface current response is dominated by an ultrafast charge transfer along the Se-Bi bonds. In contrast, photon-helicity-dependent photocurrents are found to be orders of magnitude smaller than expected from generation scenarios based on asymmetric depopulation of the Dirac cone. Our findings are of direct relevance for broadband optoelectronic devices based on topological-insulator surface currents.

¹Fritz Haber Institute of the Max Planck Society, 14195 Berlin, Germany. ²PGI-9 and JARA-FIT, Forschungszentrum Jülich, 52425 Jülich, Germany.

³Institute of Electronic Materials Technology, 01-919 Warsaw, Poland. ⁴Laboratoire des Solides Irradiés, Ecole Polytechnique, CNRS, CEA, Université Paris-Saclay, 91128 Palaiseau cedex, France. ⁵Institut für Physik, Ernst-Moritz-Arndt-Universität Greifswald, 17489 Greifswald, Germany. Correspondence and requests for materials should be addressed to L.B. (email: braun@fhi-berlin.mpg.de) or to T.K. (kampfrath@fhi-berlin.mpg.de).

Many efforts in current solid-state research aim at pushing the speed of electronic devices from the gigahertz to the terahertz (1 THz = 10^{12} Hz) range¹ and at extending their functionalities by the spin of the electron². In these respects, three-dimensional topological insulators (TIs) are a highly promising material class. Although having an insulating bulk, their surface is metallic due to a band inversion that is topologically protected against external perturbations. Bi₂Se₃ is a model TI³ as its surface features a single pair of linear Dirac-type electronic energy bands⁴ with spin-velocity locking and forbidden 180° backscattering⁵. These properties are ideal prerequisites to induce large spin polarizations by means of surface currents.

Part of this considerable potential was demonstrated by recent works, which reported the exciting possibility of launching TI surface currents by simply illuminating the sample with light^{6–13}. The direction of the photocurrent could be controlled through the polarization state of the incident light beam. The assignment to a surface process was supported by picosecond time-of-flight measurements¹³ showing that the photoinduced carriers were propagating at a speed comparable to the band velocity of the Dirac states. There is, however, still an intense debate about mechanisms leading to TI surface photocurrents. Scenarios based on asymmetric depopulation of the Dirac cone⁶ transitions into other higher-lying cones¹³, and asymmetric scattering of electrons⁸ have been proposed. To directly resolve the generation of TI surface photocurrents, we need to boost the time resolution of the experiment from so far as ~250 fs and longer^{9–13} to the scale of elementary scattering events, which can be shorter than 10 fs.

Here, we use ultrabroadband terahertz (THz) emission spectroscopy^{14–16} from 0.3 to 40 THz to probe the ultrafast evolution of photocurrents in the Ca-doped model TI Bi₂Se₃ with unprecedented time resolution. On the basis of an analysis of their temporal structure and symmetry, we identify distinct current sources. First, a slow drift current of photoinduced bulk charge carriers along the TI surface field is found. Second, we observe that currents depending on the pump helicity are orders of magnitude smaller than expected from the photocurrent generation scenario based on asymmetric depopulation of the Dirac cone⁶. This remarkable result suggests a strong mutual cancellation of the contributions of the various optical transitions, much reduced matrix elements for surface-to-bulk transitions and/or relatively small pump-induced changes in the electron band velocity. Finally, for the first time, we observe a new type of photocurrent, a surface shift current, which originates from an instantaneous displacement of electron density along the Se–Bi bond. This charge transfer is localized in a surface region of ~2 nm thickness, the natural confinement scale of topological surface states. Its relaxation time of 22 fs provides the timescale on which the optically excited surface carriers relax to an isotropic distribution. In terms of applications, the instantaneous electric field generated by the shift current could be used to drive highly spin-polarized THz electric currents at the TI surface along an easily tunable direction.

Results

Ultrafast photocurrent amperemeter. A schematic of our experiment is depicted in Fig. 1a. A femtosecond laser pulse is incident on the specimen and launches a transient charge density $j(z,t)$. This photocurrent, in turn, emits an electromagnetic pulse with transient electric field $E(t)$, in particular, covering frequencies up to the THz range, as expected from the inverse duration of the femtosecond stimulus. The measurement of $E(t)$ over a large bandwidth (0.3 to 40 THz) permits extraction

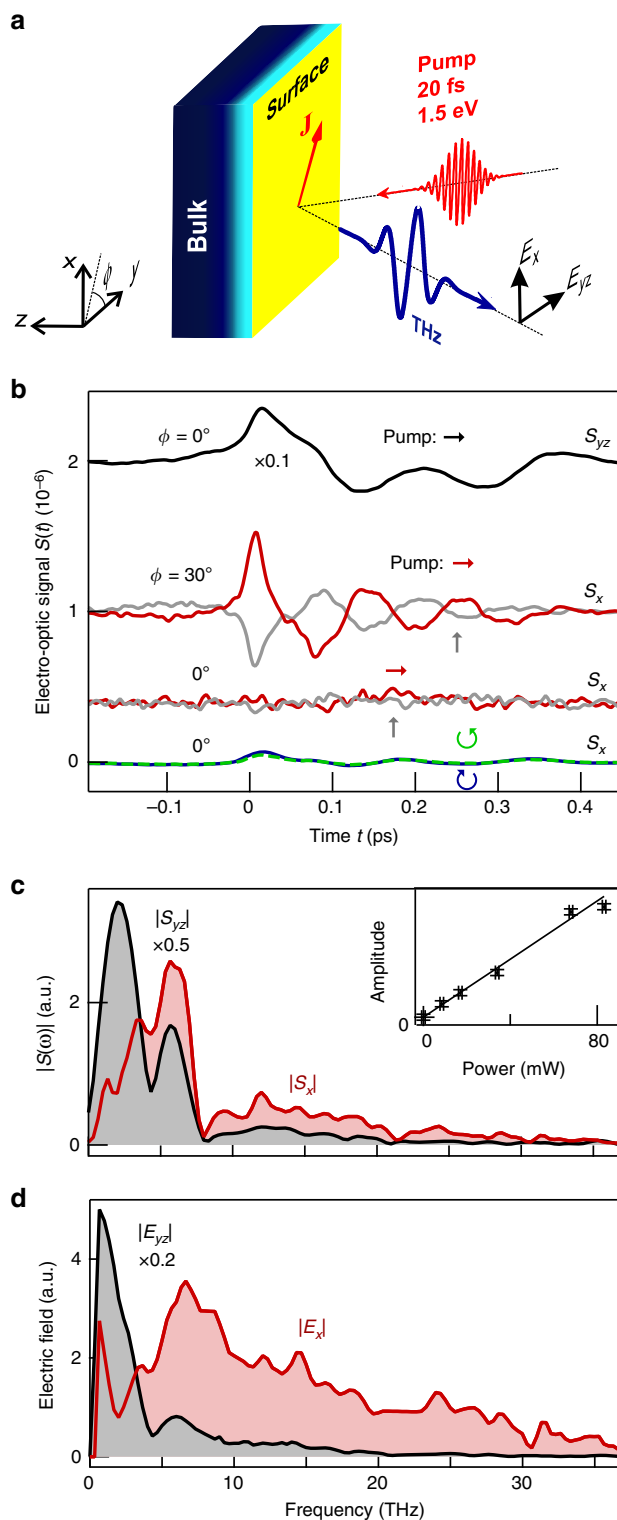


Figure 1 | THz emission experiment and raw data. (a) Schematic of the ultrafast photocurrent amperemeter. A Bi₂Se₃ crystal is excited by a femtosecond laser pulse, resulting in a photocurrent burst and, consequently, emission of a THz electromagnetic pulse. Measurement of the transient THz electric field components $E_x(t)$ and $E_{yz}(t)$ by electro-optic sampling provides access to the sheet current $\mathbf{J}(t)$ flowing inside the sample. (b) Typical x- and yz-polarized THz electro-optic signals S_x and S_{yz} measured for various settings of pump polarization and sample azimuth ϕ . The signals are offset for clarity. (c) Amplitude spectra of the THz signal and (d) THz electric field directly behind the sample as extracted from b.

of the sheet current density

$$\mathbf{J}(t) = \int dz \mathbf{j}(z, t) \quad (1)$$

with ultrafast time resolution.

As detailed in the ‘Methods’ section, this approach allows us to separately determine the current component J_x directed along the x axis and the component J_{yz} , which is a linear combination of the roughly equally weighted Cartesian components J_y and J_z (see Fig. 1a and the ‘Methods’ section). By virtue of a generalized Ohm’s law, the currents J_x and J_{yz} are, respectively, connected to the s -polarized electric-field component E_x and the perpendicular, p -polarized component E_{yz} directly behind the sample (Fig. 1a). The THz near-fields E_x and E_{yz} are obtained by measuring the THz far-field using electro-optic sampling, resulting in the electro-optic signals S_x and S_{yz} , respectively (see the ‘Methods’ section). THz waveforms are acquired at the shot-noise limit of the setup and for various settings of the pump polarization and sample azimuth ϕ (Fig. 1b).

We use this approach to study a freshly cleaved, n-type, Ca-doped Bi_2Se_3 single crystal in ambient air (see the ‘Methods’ section). While dipolar photocurrents in the inversion-symmetric crystal bulk (space group D_{3d}^5) cancel, optical excitation can in principle launch a current at the surface (space group C_{3v})¹⁷. The surface region can be thought to consist of the air–crystal interface with locally relaxed lattice structure, which overlaps with the Dirac surface states (thickness of ~ 2 nm)^{18,19}, followed by a space-charge region with bent bulk bands (thickness of tens of nanometres)^{20,21}. As the sample thickness (> 300 μm) is much larger than the pump penetration depth (24 nm; ref. 20), the front but not the back surface of the sample is probed. Further details on sample properties and characterization can be found in the ‘Methods’ section.

In what follows, we will show that our broadband current measurements allow us to discriminate different types of photocurrents and their generation in the various surface regions. This goal is achieved by first identifying two dominating components in the THz emission signal using symmetry analysis. Finally, on the basis of their temporal structure and symmetry, the two underlying photocurrent components are assigned to microscopic generation scenarios.

Raw data. Typical THz electro-optic signal waveforms $S(t)$ obtained from our Bi_2Se_3 sample are shown in Fig. 1b. The THz waveforms depend sensitively on the setting of the THz polarization (x versus yz), the pump polarization and the sample azimuthal angle ϕ . The signal amplitude grows linearly with increasing pump power, without any indication of saturation (inset of Fig. 1c). This behaviour implies that the number of excited carriers is proportional to the incident photon number.

As detailed in the following, we make the striking observation that the x - and yz -polarized components of the emitted THz field (and, thus, J_x and J_{yz}) behave very differently in terms of their magnitude (Fig. 1b), temporal shape (Fig. 1b), their behaviour after sample cleavage (Fig. 2) and their dependence on the sample azimuth ϕ (Fig. 3b). First, as seen in Fig. 1b, S_{yz} exhibits much larger amplitude than S_x but evolves significantly more slowly. Accordingly, the amplitude spectrum of S_x exhibits a larger bandwidth than S_{yz} (Fig. 1c). This trend becomes even clearer when we apply an inversion procedure to these data to extract the transient THz fields E_x and E_{yz} directly behind the sample (see the ‘Methods’ section). The resulting spectral amplitudes are displayed in Fig. 1d as a function of angular frequency ω and show that $|E_x(\omega)|$ is much broader than $|E_{yz}(\omega)|$, indicating much faster temporal dynamics. The spectrum exhibits features such as

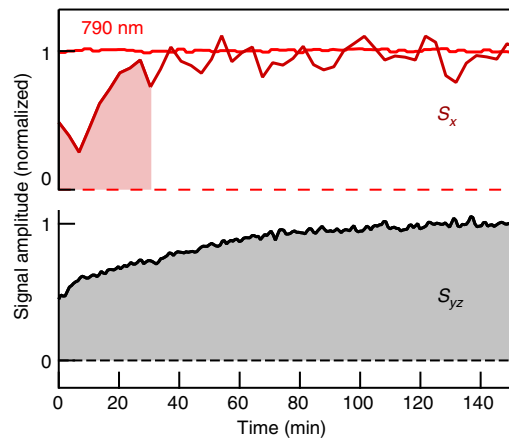


Figure 2 | Long-term signal changes. Evolution of the amplitudes of THz signals S_x and S_{yz} and the reflectance of the 790 nm pump beam following cleaving of the sample. The constant 790 nm signal indicates that no sample damage occurs.

the dips of $|E_x(\omega)|$ at $\omega/2\pi = 2$ THz and 4 THz whose origin becomes clear further below.

Second, to investigate the impact of surface modification on S_x and S_{yz} , we freshly cleave the sample and subsequently acquire THz signals continuously over > 2 h with the sample exposed to air. While the shape of the THz waveforms does not undergo measurable modifications, their global amplitude increases by a factor of ≈ 2 in the course of time (Fig. 2). Note this rise proceeds within 30 min for S_x but significantly slower (within 100 min) for S_{yz} . We will later use this different evolution speed of S_x and S_{yz} to draw conclusions concerning the degree of surface localization of the currents J_x and J_{yz} . In contrast to S_x and S_{yz} , measurable changes of the sample reflectance at a wavelength of 790 nm are not observed, thereby ruling optical degradation of our sample out. In addition, we did not observe temporal changes in the signal symmetry, which is discussed in the next section.

Signal symmetries. In addition to their different amplitude and temporal structure, S_x and S_{yz} also depend very differently on the sample azimuth ϕ . To quantify this behaviour, we measure waveforms $S_x(t, \phi)$ and $S_{yz}(t, \phi)$ for an extended set of ϕ -values, example traces of which are shown in Fig. 3a. To reliably extract an average signal amplitude for each ϕ , we project the time-domain signal on a suitable reference waveform (see the ‘Methods’ section). The resulting signal amplitude as a function of ϕ is displayed in Fig. 3b. While both S_x and S_{yz} exhibit a 120° -periodic component of comparable magnitude, S_{yz} has a much larger and dominant component independent of ϕ .

The three-fold rotational symmetry of the THz signals is fully consistent with the symmetry groups of sample surface and bulk as shown by a detailed analysis of the second-order conductivity tensor (see the ‘Methods’ section)³. Importantly, it allows us to significantly reduce the large amount of experimental data contained in $S(t, \phi)$: for a given THz polarization (x or yz) and pump polarization, each two-dimensional set $S(t, \phi)$ can be written as a linear combination of just three basis functions (see the ‘Methods’ section),

$$S(t, \phi) = A(t) + B(t)\sin(3\phi) + C(t)\cos(3\phi). \quad (2)$$

Therefore, three basis signals $A(t)$, $B(t)$ and $C(t)$ fully characterize the entire data set $S(t, \phi)$. They are, respectively, obtained by projecting $S(t, \phi)$ onto the mutually orthogonal functions 1, $\sin(3\phi)$ and $\cos(3\phi)$ (see the ‘Methods’ section). Extracted waves

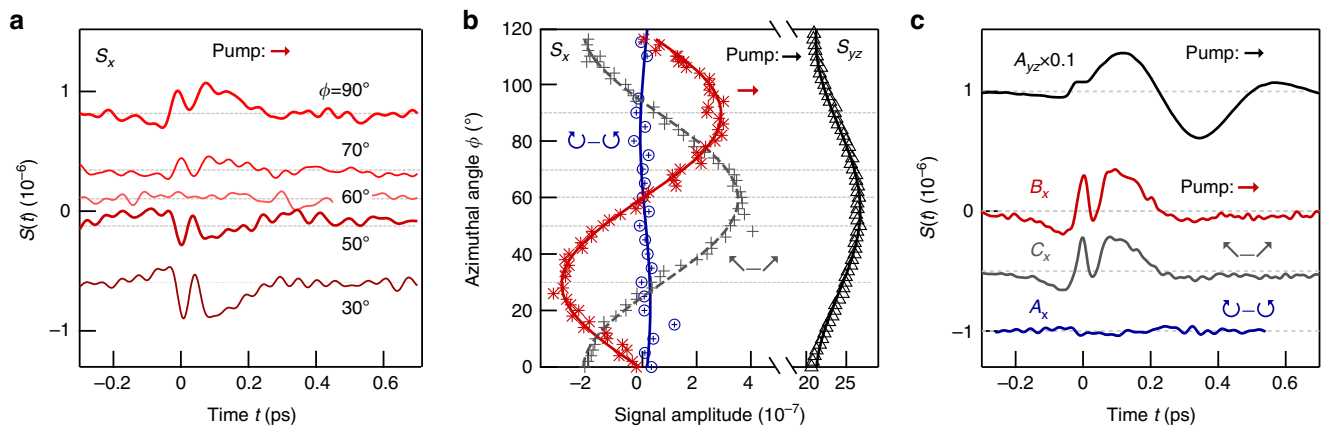


Figure 3 | Azimuth dependence and dominant components of THz signal S_x . (a) THz signal waveforms at various sample azimuth angles ϕ and for fixed pump polarization. (b) Extracted THz amplitude versus ϕ for various pump-polarization settings (\rightarrow and differential signals \leftarrow and \ominus – \oplus). While both S_x and S_{yz} exhibit a 3ϕ -type-dependent component of comparable magnitude, S_{yz} has a much larger and dominant component independent of ϕ . (c) Dominant temporal components of signal sets $S_{yz}(t, \phi)$ and $S_x(t, \phi)$ for various pump polarizations, extracted by using equation (2) (see the ‘Methods’ section).

are shown in Fig. 3c and Supplementary Fig. 1d for the two THz polarizations and various pump polarizations.

We begin with considering the impact of the pump helicity on the photocurrent. The bottommost curve in Fig. 3c represents the ϕ -independent component $A_x(t)$ of the difference of the signals taken with right-handed (\odot) and left-handed (\ominus) circularly polarized pump light. The amplitude of this waveform is comparable to the noise floor. In other words, a helicity-dependent yet simultaneously ϕ -independent THz signal is small and below our detection threshold. This notion is consistent with time-domain raw data (blue versus green trace in Fig. 1b) and the absence of an offset in the ϕ -dependence (blue curve of Fig. 3b). An analogous behaviour is observed for THz signals S_{yz} (see Supplementary Fig. 2). We note that such small magnitude of the pump-helicity-dependent and ϕ -independent photocurrent does not contradict the previously reported observation of time-integrated currents⁶ as will be addressed in the ‘Discussion’ section.

Ultrafast photocurrents. Figure 3c leads to another important conclusion of our symmetry analysis: regardless of the pump polarization, all signals S_x and S_{yz} are, respectively, dominated by just one fast and one slow waveform. We use these signals to extract the underlying source currents (see the ‘Methods’ section), which are displayed in Fig. 4a. After an initial onset, both J_x and J_{yz} change sign, indicating a backflow of charge. Note, however, J_x proceeds much faster than J_{yz} : the rise time from 10 to 90% of the current maximum is 16 and 40 fs for J_x and J_{yz} , respectively. Subsequently, J_x decays with a time constant of 22 fs, while J_{yz} decays within 700 fs.

To determine the origin of J_x and J_{yz} based on their ultrafast dynamics, we briefly review known photocurrent generation mechanisms^{6,8,22–27}. In general, optical excitation transfers electrons from initial states $|i\rangle$ into final states $|f\rangle$ (Fig. 4b), followed by relaxation processes such as scattering into other states, phonon emission and recombination²⁸. Photocurrents can arise in both regimes, that is, during the optical transition and during the subsequent relaxation. As our pump photon energy (1.57 eV) is much larger than the Bi_2Se_3 band gap, numerous vertical interband transitions are allowed²⁹ (Fig. 4f) and expected to outnumber the contribution of phonon- or impurity-assisted nonvertical transitions³⁰. In the subsequent relaxation regime, currents can arise from, for instance, scattering by a

noncentrosymmetric potential⁸, asymmetric recombination³¹ and carrier acceleration in an intrinsic surface field (drift current)^{32,33}. In all the cases, inversion symmetry needs to be broken to obtain a macroscopic dipolar net current.

Drift current. As seen in Fig. 4a, the slow current $J_{yz}(t)$ has a rise time (40 fs) significantly slower than the duration of the excitation pulse (≈ 20 fs). Therefore, it cannot arise from the initial optical transition. In fact, previous works on Bi_2Se_3 assigned the slow J_{yz} component to a carrier drift in the surface field, consistent with the strong dependence of J_{yz} on the doping level of Bi_2Se_3 (refs 9–11). This notion is further supported by additional observations made in our experiment: first, the initial electron flow is directed toward the sample surface, along the direction of the space-charge field of our effectively n-doped sample. Second, the 40 fs rise time (Fig. 4a) is on the order of the bulk Drude scattering time of our sample (~ 18 fs, see the ‘Methods’ section) that limits charge acceleration in the surface field.

Following its initial rise, J_{yz} is found to change sign. Plasma oscillation³⁴ of the charge carriers cannot account for this feature because the short Drude scattering time (~ 18 fs, see the ‘Methods’ section) would strongly attenuate such dynamics in less than 100 fs, in contrast to our observation. We consequently assign the sign change of J_{yz} to the backflow of charge that accompanies the overall relaxation of the photoexcited system back to the equilibrium state. From photoemission studies²⁸, the relaxation of optically excited bulk carriers is known to occur on a timescale of 1 ps, in agreement with the relaxation time of J_{yz} (see Fig. 4a).

Shift current. Having assigned the slow, dominant part of current J_{yz} , we now focus on the very fast, sub-100 fs dynamics of the photocurrent J_x . Concerning immediate photocurrent generation by an optical transition $|i\rangle \rightarrow |f\rangle$, Sipe and colleagues^{22,35} used perturbation theory and identified three distinct mechanisms: injection currents, shift currents and optical rectification^{22,36}. Injection currents J_{inj} arise because initial and final state of the perturbed electron have different band velocity. An example is the asymmetric band depopulation scenario⁶ shown in Fig. 4b: a circularly polarized pump excites electrons from the Dirac cone into higher-lying states with different band slope (group velocity). Therefore, for short enough excitation, J_{inj} should rise instantaneously to a magnitude that scales with the average

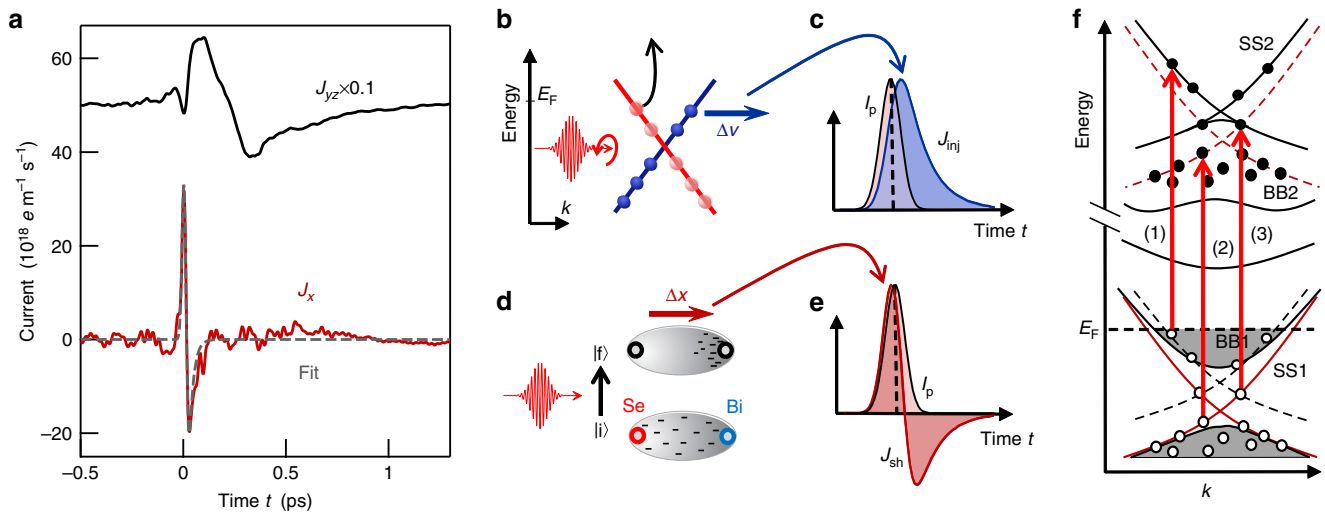


Figure 4 | Extracted photocurrents and their assignment. (a) Source currents of the two dominant signal components (see Fig. 3). The dynamics of these currents allow us to reveal the origin of the photocurrent. Curves are offset for clarity. (b) Example of an injection-type photocurrent. The pump pulse promotes electrons from the Dirac cone into other bands, thereby changing the electron band velocity. An asymmetric depopulation of the Dirac cone and, thus, nonzero net current is achieved by using circularly polarized light⁶. (c) Typical shape of the resulting photocurrent $J_{inj}(t)$. Here, $I_p(t)$ is the intensity envelope of the laser pulse. (d) Scenario of a shift photocurrent arising from an ultrafast transfer of electron density along the Se-Bi bond. (e) Typical bipolar temporal shape of the resulting sheet current $J_{sh}(t)$. (f) Schematic of the electronic band structure of Bi_2Se_3 . While BB1/BB2 represent bulk bands below/above the Fermi level E_F , SS1/SS2 refer to surface states. Red arrows indicate three examples of pump-induced optical transitions (photon energy of ~ 1.5 eV). To better illustrate the excitation process, thin black/red lines indicate copies of SS1/SS2 shifted upwards/downwards by the pump photon energy. Ground-state occupation is displayed shaded.

velocity change Δv and the density N of the excited electrons. In this simplified model, the resulting current is

$$J_{inj} = \sigma_{inj} \Delta v \cdot \left[\Theta(t) e^{-t/\tau_{inj}} \right] * I_p \quad (3)$$

where the initial sheet charge density $\sigma_{inj} = eN\Delta z_{inj}$ is proportional to the thickness Δz_{inj} of the emitting sheet, and $\Theta(t)$ is the unit step function. Note that relaxation processes such as electron scattering are not covered by the theory of ref. 22. We have introduced them phenomenologically by an exponential decay with time constant τ_{inj} . Backflow of electrons is diffusive³⁷ and ignored on the short timescales considered here. Finally, the convolution (denoted by $*$) with the pump intensity envelope $I_p(t)$ (normalized to unity) accounts for the shape of the pump pulse, resulting in a current with the typical temporal shape shown in Fig. 4c.

Shift currents³⁸, on the other hand, arise when the electron density distribution of the excited state $|f\rangle$ is spatially shifted with respect to $|i\rangle$ (Fig. 4d). For short excitation, this process leads to a step-like charge displacement $\Delta x_{sh} \Theta(t)$ whose temporal derivative is proportional to the shift current J_{sh} . With arguments analogous to the injection case, we obtain

$$J_{sh} = \sigma_{sh} \Delta x \frac{\partial}{\partial t} \left[\Theta(t) e^{-t/\tau_{sh}} \right] * I_p, \quad (4)$$

with $\sigma_{sh} = eN\Delta z_{sh}$. This model implies J_{sh} initially follows the profile of $I_p(t)$ and becomes bipolar if the relaxation time τ_{sh} is comparable to or longer than the pump duration (Fig. 4e).

Finally, optical rectification can be understood as a transient, nonresonantly driven charge displacement that follows the intensity envelope of the pump pulse. It arises from all transitions between the initial and final states whose energy difference is different from the incident photon energy of 1.57 eV (ref. 39). To evaluate the relative importance of optical rectification in our experiment, we compared the emitted THz amplitude of our TI sample with that of a pump-transparent ZnTe(110) crystal, which is known for relatively strong optical rectification at the

pump photon energy used here⁴⁰. We find that, normalized to the thickness of the emitting crystal, the THz signal S_x from the TI sample is about two orders of magnitude larger than that from ZnTe. Therefore, optical rectification in Bi_2Se_3 is expected to make a negligible contribution, and we are left with considering ultrafast injection and shift currents.

Note the characteristic shape of J_{inj} and J_{sh} is very distinct: unipolar (Fig. 4c) versus bipolar asymmetric (Fig. 4e). Having understood how the temporal shape of a current is intrinsically linked to its origin, we now look for such fingerprints in our data (Fig. 4a). Indeed, we find that the measured photocurrent J_x (Fig. 4a) has bipolar asymmetric temporal shape: the signature of a shift current. In addition, fitting equation (4) to J_x yields excellent agreement (Fig. 4a) for a pump duration of 23 fs, $\tau_{sh} = 22$ fs and $\Delta x_{sh} \Delta z_{sh} \approx 36 \text{ \AA}^2$. In this procedure, we use the excitation density ($N = 6.9 \times 10^{24} \text{ m}^{-3}$) as inferred from the absorbed pump fluence ($4 \mu\text{J cm}^{-2}$), the pump photon energy (1.57 eV) and the pump penetration depth (24 nm at 1/e intensity)²⁰. The amplitude spectrum of the calculated J_{sh} peaks at 6 THz (not shown), consistent with the peak position of the measured E_x amplitude spectrum (Fig. 1d).

One could argue that the current J_x is not a pure shift current (Fig. 4e) but still contains a component arising from a rapidly decaying injection current (Fig. 4c). We can exclude this possibility based on a symmetry analysis and photocurrent theory work²². For example, for linear pump polarization at 45° with respect to the plane of incidence, the resulting current J_x is solely related to the second-order conductivity tensor element σ_{xyy} (see the ‘Methods’ section and Supplementary Note 1). As dictated by symmetry, this element equals σ_{yyx} and becomes, therefore, real-valued when the photocurrent frequency approaches $\omega = 0$. From the microscopic analysis of Nastos and Sipe²², it follows that this tensor element and the related photocurrent J_x are not due to an injection current, provided that photocurrent frequencies ω higher than the current relaxation rate are considered (see the ‘Methods’ section).

Surface localization. Our photocurrent measurements and analysis directly reveal an ultrafast shift current and a drift current in the time domain. It is so far, however, unclear to which extent these currents are localized at the surface. Since the photocurrent observed here is a quadratic nonlinear-optical effect (see inset of Fig. 1c), it only flows in regions where inversion symmetry is locally broken⁴¹. In our sample, this breaking arises from two perturbations of the inversion-symmetric bulk: (i) the surface, which extends over the first 1 to 2 quintuple layers (~ 1 to 2 nm) as indicated by the thickness of surface states¹⁸ and the depth of surface lattice relaxation,¹⁹ and (ii) the space-charge field E_{SC} , which points along the surface normal and extends ~ 15 nm into the depth of the sample, as implied by an estimate analogous to ref. 20.

Since the slow component of J_{yz} is a drift current of photoexcited carriers in the space-charge field^{9–11}, it is also localized in a depth of ~ 15 nm. In addition, its amplitude changes during sample aging must arise from gradual modifications of E_{SC} (Fig. 2). If J_x were also dominated by E_{SC} , its amplitude should evolve analogously to J_{yz} following sample cleaving. In contrast, we observe that J_x evolves about five times faster than J_{yz} (see Fig. 2) such that J_x cannot arise from perturbation (ii) but rather from the remaining perturbation (i). Therefore, the shift current is localized in the first one to two quintuple layers of the Bi_2Se_3 surface. The resulting Δz_{sh} of less than 2 nm and the above extracted estimate for $\Delta x_{sh}\Delta z_{sh}$ imply that the shift distance Δx_{sh} is on the order of 1 Å.

We note that the THz emission spectra exhibit sharp features at 2 and 4 THz (Fig. 1c,d) which coincide with the frequencies of long-wavelength bulk phonon modes at 1.9, 2.1 and 4 THz (ref. 42). While the 1.9 THz mode is infrared-active and can thus absorb pump-generated THz radiation, the 4 THz mode is exclusively Raman active in the inversion-symmetric bulk. Therefore, the presence of the 4 THz feature in the emission spectrum suggests this mode is infrared-activated in the TI surface region where inversion symmetry is locally broken⁴³. This effect further underlines the surface sensitivity of THz emission spectroscopy.

Discussion

Summarizing our results, we have shown that our ultrabroadband THz emission data are fully consistent with the notion that (i) the photocurrent J_x arises from an instantaneous photo-induced shift of charge density by ~ 1 Å in an ~ 2 nm thick surface region of Bi_2Se_3 . The displacement relaxes on a very fast timescale of 22 fs. The much slower current J_{yz} is dominated by a drift current of optically excited carriers in the surface field. (ii) A pump-helicity-dependent and simultaneously azimuth-independent photocurrent is smaller than our detection threshold of $10^{18} \text{ e m}^{-1} \text{ s}^{-1}$. This assertion is also valid for other injection-type transport scenarios such as photon-drag currents⁴⁴. It is instructive to discuss these observations and compare them with previous works.

Finding (i) represents the first observation of a surface shift current, which was predicted by Cabellos *et al.*⁴⁵ very recently. We note that we also observe signatures of ultrafast surface shift currents in other TI samples, including thin films⁴⁶ of Bi_2Se_3 and Bi_2Te_3 (not shown). We emphasize that revealing the time-domain fingerprint of shift currents relies on the 20 fs time resolution of our experiment. Longer pump pulses can easily obscure this signature, even in materials with broken bulk inversion symmetry³⁶. The surface shift current is probably the source of the linear photogalvanic surface currents that have been reported previously⁶, but not assigned.

Our results show that the displacement of bound charges occurs in a sheet with thickness $\Delta z_{sh} \sim 2$ nm, which is the

thickness of the layer where the Dirac states are expected to dominate charge transport¹⁸. This notion is consistent with reports¹⁹ showing that only the first quintuple layer exhibits inversion asymmetry on the order of 10%. The shift distance $\Delta x_{sh} \sim 1$ Å compares well with reported charge shifts on the order of the bond length (~ 3 Å) in noncentrosymmetric semiconductors³⁸.

The three-fold azimuthal symmetry of J_x (Fig. 3b) suggests the electron density is displaced along the 120°-ordered p-type Se–Bi bonds⁴⁷. In fact, previous studies have shown that the electron density associated with the Dirac states is known to shift gradually from Se toward Bi atoms when energies below and above the Dirac point are considered^{3,47,48}. As Bi and Se atoms lie in different layers, the Bi–Se bond forms an angle of about 45° with respect to the sample surface normal. Therefore, the shift current also has a z-component with a strength comparable to J_x , consistent with the sharp peak present in J_{yz} at $t = 0$ fs (see Fig. 4a and Supplementary Fig. 1d).

In principle, the ultrafast Se–Bi charge transfer can be driven by all kinds of optical transitions involving surface states. Examples of possible transitions induced by the 1.57 eV pump photons are shown in Fig. 4f: (1) surface-to-bulk, (2) bulk-to-surface and (3) surface-to-surface (intercone) transitions. Following excitation, the charge carriers undergo multiple scattering processes, finally resulting in an isotropic distribution. The time constant (22 fs) of this process found here is consistent with other measurements of anisotropy relaxation at the TI surface: ultrafast optical Kerr effect (time constant of ~ 25 fs)⁴⁹ and equilibrium transport experiments (substantially smaller than 300 fs, see Supplementary Note 2)^{50,51}. Note that due to spin-momentum locking at the TI surface, the decay of the anisotropy of the charge-carrier distribution is strongly connected with the decay of the transient surface spin polarization⁵². The timescales of these processes are much shorter than that of the energy relaxation of the surface charge carriers (~ 1 ps; ref. 28).

Result (ii), the absence of a pump-helicity-dependent photocurrent, is surprising and imposes significant constraints on the generation mechanism of this current. We first note this result is consistent with the photocurrent magnitudes found by previous electrode-based time-integrating⁶ and picosecond-resolved¹³ measurements. From these works, it follows that under excitation conditions similar to ours, the pump-helicity-dependent photocurrent reaches a peak value that is slightly below the detection threshold $10^{18} \text{ e m}^{-1} \text{ s}^{-1}$ of our setup (see Supplementary Note 3).

It is instructive to compare the upper photocurrent limit set by our experiment to a recently suggested microscopic scenario⁶ in which the pump-helicity-dependent photocurrent arises from asymmetric depopulation of the Dirac cone by optical transitions into rapidly decaying bulk states (Fig. 4b). On the basis of this injection-type scenario, we use equation (3) to estimate the initial ballistic sheet-current density as $Nv_D\Delta z_D$, where $v_D = 0.5 \text{ nm fs}^{-1}$ is the band velocity in the Dirac cone²⁸, $\Delta z_D = 2$ nm the thickness of the Dirac states¹⁸ and N is the bulk excitation density. The resulting magnitude of $10^{22} \text{ e m}^{-1} \text{ s}^{-1}$ is four orders of magnitude larger than the maximum current measured in our experiment.

Possible reasons why the photocurrent magnitude predicted by this plausible scenario so drastically exceeds the actually measured pump-helicity-dependent photocurrent are as follows. First, matrix elements for bulk–surface optical transitions are much smaller than for bulk–bulk transitions. In other words, light absorption is much more pronounced in the bulk than at the surface, in contrast to the tacit assumption of homogeneous absorptivity made in the estimate above. Second, the band velocity of initial and final state are approximately equal

(see equation (3)). Finally, there is a great deal of cancellation when summing over the contributions of all optical transitions. Indeed, as shown theoretically, a zero net current results when only optical transitions within the Dirac cone are considered⁵³. Experiments using pump pulses with tunable pump photon energy^{54,55} will likely provide more insights into the nature of the pump-helicity-dependent photocurrent, in particular, in terms of intracone and below-gap optical transitions^{24,53,54}.

In conclusion, we have measured the dynamics of ultrafast photocurrents on the surface of the Ca-doped three-dimensional model TI Bi₂Se₃ with a time resolution as short as 20 fs. We find that the peak amplitude of pump-helicity-dependent photocurrents is much smaller than predicted by a recent model based on asymmetric optical transitions between Dirac-cone and bulk states⁶. For the first time, we have observed a surface shift photocurrent, which arises from a charge displacement at the TI surface. The fast decay time (22 fs) of this current attests to the rapid loss of charge-carrier surface anisotropy. On a more applied note, the shift current is potentially interesting for ultrafast optical manipulation of the TI surface, thereby ultimately modifying its topological properties⁵⁶. The local electric field generated by the shift current could be used to drive highly spin-polarized THz electric currents at the TI surface. The direction of this secondary current could easily be controlled by the pump-beam polarization, thereby opening up new possibilities to access the TI surface states. Finally, our results highlight broadband THz emission spectroscopy as a novel and highly sensitive probe of surfaces.

Methods

Sample details. Single crystals of Ca-doped Bi₂Se₃ were grown by the Bridgman–Stockbarger method by pulling a sealed quartz ampoule in a vertical temperature gradient. A fresh surface is obtained by cleaving using adhesive tape. The dimensions of the sample used for THz emission spectroscopy are approximately $2 \times 3 \times 0.3$ mm³.

For characterization of the sample by angle-resolved photoelectron spectroscopy (ARPES), the sample was studied directly after cleaving under ultrahigh-vacuum conditions (pressure 2×10^{-10} mbar) and, a second time, after exposing the sample to an ambient-pressure atmosphere of N₂ for a few seconds. ARPES measurements on the N₂-exposed surface confirm the presence of Dirac surface states with the Fermi energy located roughly 100 meV above the bulk conduction band minimum (see Supplementary Fig. 3). From these data, a conduction-band electron mass of 0.115 bare electron masses is inferred⁵⁷.

Hall measurements⁵⁸ yield a bulk hole density of 1.34×10^{17} cm⁻³ and a mobility of 275 cm² V⁻¹ s⁻¹. Using these values, the effective mass inferred from ARPES data and the Drude formula, we extract a velocity relaxation time of 18 fs in the bulk material.

Ultrafast THz emission setup. Laser pulses (duration of ≈ 20 fs, centre wavelength of 790 nm, energy 1 nJ) from a Ti:sapphire oscillator (repetition rate of 80 MHz) are focused onto the sample (beam diameter of 200 μ m full-width at half intensity maximum) under 45° angle of incidence, resulting in an average intensity < 0.3 kW cm⁻², well below sample damage threshold. The specularly emitted THz pulse is focused onto an electro-optic crystal in which the THz electric field is detected by broadband electro-optic sampling⁴⁰. We use a (110)-oriented GaP crystal (thickness of 250 μ m) owing to its relatively flat and broadband response function¹⁶. The only exceptions are the measurements of the two-dimensional data set $S(t, \phi)$ (Fig. 3 and Supplementary Fig. 1), which are sped up by using a (110)-oriented ZnTe crystal (thickness of 300 μ m), which exhibits an enhanced detector response at the expense of reduced bandwidth. To calibrate the direction of the measured photocurrent, we use a photoconductive switch as a reference emitter in which the direction of the initial photocurrent burst is along the direction of the external bias field.

Optical wave plates are used to set the polarization state of the pump pulse to linear (with arbitrary rotation angle) or circular. Here, it is essential to avoid any optically birefringent elements (including mirrors) between wave plate and sample. A THz wire-grid polarizer (field extinction ratio of 10^{-2}) allows us to measure the x - and y -components E_x and E_{yz} of the THz electric field separately, thereby disentangling current components J_x and J_{yz} , the latter being a linear combination of J_y and J_z (see Fig. 1a and equation (8)). To ensure the electro-optic THz detector has an identical response to E_x and E_{yz} , a wire-grid polarizer with 45° orientation is placed in front of it. Variation of the sample azimuth ϕ is performed by attaching the sample to a computer-controlled rotation stage.

From THz signals to THz fields. To proceed from the measured electro-optic signal $S(t)$ to the THz electric field $E(t)$ directly above the sample surface, we note that there is a linear relationship between the two quantities. For example, in the frequency domain, the THz field component E_x and the corresponding signal S_x are connected by the transfer function $h(\omega)$ through the simple multiplication

$$S_x(\omega) = h(\omega)E_x(\omega). \quad (5)$$

A completely analogous relationship is valid for E_{yz} and S_{yz} . We measure the transfer function of our setup by using 50 μ m thick GaP(110) as a reference emitter placed before the TI sample that has been substituted by an Ag mirror. Details of the shape of the transfer function are shown in Supplementary Fig. 4 and discussed in the Supplementary Note 4.

From THz fields to THz currents. To finally obtain the source current $J(t)$ from the THz electric field $E(t)$ measured directly above the sample surface, we make use of the following generalized Ohm's law³⁴:

$$E_x(\omega) = -\frac{Z_0}{\cos \alpha + \sqrt{n^2 - \sin^2 \alpha}} J_x(\omega) \quad (6)$$

$$E_{yz}(\omega) = -\frac{Z_0 \sqrt{n^2 - \sin^2 \alpha}}{n^2 \cos \alpha + \sqrt{n^2 - \sin^2 \alpha}} J_{yz}(\omega). \quad (7)$$

Here, $\omega/2\pi$ is the THz frequency, $Z_0 \approx 377 \Omega$ is the vacuum impedance, $n(\omega)$ is the refractive index of Bi₂Se₃ taken from ref. 50, $\alpha = 45^\circ$ is the angle of incidence, and

$$J_{yz}(\omega) = J_y(\omega) - \frac{\sin \alpha}{\sqrt{n^2 - \sin^2 \alpha}} J_z(\omega) \quad (8)$$

is a weighted sum of the currents flowing along the y and z directions. For Bi₂Se₃ and frequencies above 5 THz, the weighting factor $\sin \alpha / \sqrt{n^2 - \sin^2 \alpha}$ of J_z is on the order of 0.3. The inverse Fourier transformation of the resulting current spectra yields the currents in the time domain (Fig. 4a).

We note that the overall magnitude of the extracted currents is subject to an estimated uncertainty on the order of 3, which arises from the cumulated effects of uncertainties of beam parameters (such as beam diameter and divergence), of the precise optical material properties (in particular, close to phonon frequencies) and from the deviations of the optical and THz beam from a perfect Gaussian profile.

Waveform mean amplitude. To characterize a complete THz waveform $S(t)$ by a single mean amplitude \bar{S} , an often-used procedure is to calculate the root-mean square $[\int dt S^2(t)]^{1/2}$. The drawback of this method is that it is based on nonlinear operations, which annihilate phase information and make the identification of additive signal components difficult. Therefore, calculation of a mean amplitude \bar{S} of a given signal should be linear with respect to $S(t)$. Our solution is to project $S(t)$ on a suitable and normalized reference waveform $S_{\text{ref}}(t)$ by means of the scalar product

$$\bar{S} = \frac{1}{N} \langle S_{\text{ref}}, S \rangle = \frac{1}{N} \int dt S_{\text{ref}}(t) S(t) \quad (9)$$

where $N = \langle S_{\text{ref}}, S_{\text{ref}} \rangle^{1/2}$ normalizes S_{ref}/N to unity. As required, this operation is linear with respect to $S(t)$ and, therefore, does not mix up additive signal components.

In the case of our two-dimensional data set $S(t, \phi)$, we use the most intense signal (with respect to ϕ) as reference. This choice is arbitrary, but we checked that other reference waveforms yield qualitatively identical results within our signal-to-noise ratio. According to equations (2) and (9), the basis functions $A(t)$, $B(t)$ and $C(t)$ of the data set $S(t, \phi)$ are then obtained by multiplying $S(t, \phi)$ with $1/2\pi$, $\sin(3\phi)/\pi$ and $\cos(3\phi)/\pi$, respectively, and subsequent integration from $\phi = 0$ to 2π .

Azimuthal symmetry analysis. The inset of Fig. 1c shows that the THz signal grows linearly with the pump power, that is, with the square of the pump field $F(t)$. Therefore, the resulting current density can phenomenologically be described by the general nonlocal relationship⁵⁹

$$j_i(\mathbf{x}, t) = \sum_{jk} \int \int \int dt_1 dt_2 d^3 \mathbf{x}_1 d^3 \mathbf{x}_2 \sigma_{ijk}(t - t_1, t - t_2, \mathbf{x} - \mathbf{x}_1, \mathbf{x} - \mathbf{x}_2) F_j(\mathbf{x}_1, t_1) F_k(\mathbf{x}_2, t_2). \quad (10)$$

Here, F_j is the j th Cartesian component of the pump field, and σ_{ijk} is a third-rank tensor field describing the quadratic material response. Upon sample rotation described by the matrix R_{ϕ} , the nonlinear response function transforms according to

$$\sigma'_{i'j'k'} = \sum_{ijk} R_{i'i} R_{j'j} R_{k'k} \sigma_{ijk}. \quad (11)$$

When we focus on rotations about the sample normal by an angle ϕ , the matrix elements R_{ϕ} are given by linear combinations of the functions 1, $\cos \phi$ and $\sin \phi$ or, equivalently, 1, $\exp(i\phi)$ and $\exp(-i\phi)$.

Since the R_{ij} show up in third order in the response transformation described by equation (11), the transformed $\sigma'_{ijk}(\phi)$ is a third-order mixed polynomial with respect to 1 , $\exp(i\phi)$ and $\exp(-i\phi)$, that is, a linear combination of the terms $\exp(im\phi)$ where the integer m runs from -3 to $+3$. From these seven terms, however, only $\exp(-3i\phi)$, $\exp(3i\phi)$ and 1 remain since our sample is invariant under rotation by $2\pi/3 = 120^\circ$ about the surface normal. In other words, $\sigma'_{ijk}(\phi)$ is a linear combination of the functions 1 , $\sin(3\phi)$ and $\cos(3\phi)$.

As seen from equations (1) and (6–8), the THz field emitted by the current-density distribution \mathbf{j} is linear with respect to \mathbf{j} with a proportionality constant that depends on the material only through the linear-optical constants at THz frequencies. Since for our sample these constants are invariant under azimuthal rotations, the ϕ -dependence of the THz signal is inherited by that of \mathbf{j} and, thus, σ'_{ijk} .

To summarize, the THz signal depends on the sample azimuth ϕ through a linear combination of the three terms 1 , $\sin(3\phi)$ and $\cos(3\phi)$ (see equation (2)). This conclusion is consistent with our experimental observations (see Fig. 3b and Supplementary Fig. 1c).

Extended symmetry analysis. While the previous subsection focused on rotations about the sample surface normal by an angle ϕ , we now also allow for variations of the pump beam's angle of incidence α and the polarization state of the pump field. By using the electric-dipole approximation and a Fourier transformation with respect to time, equation (10) yields the photocurrent-density amplitude⁵⁹

$$j_i(\mathbf{x}, \omega) = 2 \sum_{jk} \int_{\omega > 0} d\omega' \sigma_{ijk}(\mathbf{x}, \omega' + \omega, -\omega') F_j(\mathbf{x}) f_k^*(\mathbf{x}) \quad (12)$$

at THz frequency $\omega > 0$. Here, \mathbf{F} and \mathbf{f} are the complex-valued pump-field Fourier amplitudes at frequencies $\omega + \omega'$ and ω' , respectively.

The third-rank tensor σ_{ijk} is nonzero only in regions of broken inversion symmetry, that is, at the surface region of our sample. According to the C_{3v} symmetry of the sample surface, there are only five independent tensor elements: $\eta_1 = \sigma_{xxz} = \sigma_{yyz}$, $\eta_2 = \sigma_{xxz} = \sigma_{yyz}$, $\eta_3 = \sigma_{zxx} = \sigma_{zyy}$, $\eta_4 = \sigma_{yyy} = -\sigma_{yxx} = -\sigma_{xxy} = -\sigma_{yxx}$ and $\eta_5 = \sigma_{zzz}$. The other tensor elements are zero⁴¹.

If the driving field has an angle of incidence α and polarization components F_s , f_s and F_p , f_p along the directions perpendicular and in the plane of incidence, respectively, the resulting photocurrents are given by

$$j_x = -\eta_4 \cdot (F_s f_s^* - F_p f_p^* \cos^2 \alpha) \sin(3\phi) - \eta_4 \cdot (F_p f_p^* + F_s f_s^*) \cos \alpha \cos(3\phi) - (\eta_1 F_p f_s^* + \eta_2 F_s f_p^*) \sin \alpha \quad (13)$$

$$j_y = -\eta_4 \cdot (F_s f_s^* - F_p f_p^* \cos^2 \alpha) \cos(3\phi) + \eta_4 \cdot (F_p f_p^* + F_s f_s^*) \cos \alpha \sin(3\phi) - (\eta_1 F_p f_s^* + \eta_2 F_s f_p^*) \sin \alpha \cos \alpha \quad (14)$$

$$j_z = \eta_3 \cdot (F_s f_s^* + F_p f_p^* \cos^2 \alpha) + \eta_5 F_p f_p^* \sin^2 \alpha. \quad (15)$$

Here, we have omitted the frequency integral and the factor of 2 of equation (12) for brevity. These equations in conjunction with equations (1) and (6–8) show that the three-fold symmetric current contributes about equally to S_x and S_y , consistent with the observed amplitude variations seen in Supplementary Fig. 1d.

Note the tensor element $\eta_4 = -\sigma_{xxy} = -\sigma_{xyx}$ is symmetric under exchange of the last two indices. Therefore, η_4 becomes purely real-valued when the frequency approaches $\omega = 0$. On the basis of photocurrent theory work²², this property is indicative of a shift current. In contrast, injection currents require σ_{ijk} to be purely imaginary²², which implies sign inversion under exchange of the last two tensor indices. Therefore, any possible injection or pump-helicity-dependent photocurrent is related with η_1 and η_2 , and it is independent of the sample azimuth ϕ . We note these conclusions are based on the assumption of negligible current relaxation²². Therefore, they apply at frequencies ω higher than the current relaxation rates $1/\tau_{inj}$ and $1/\tau_{sh}$.

Data availability. The data sets generated and analysed during the current study are available from the corresponding authors on reasonable request.

References

- del Alamo, J. A. Nanometre-scale electronics with III-V compound semiconductors. *Nature* **479**, 317–323 (2011).
- Stamps, R. L. *et al.* The 2014 magnetism roadmap. *J. Phys. D Appl. Phys* **47**, 333001 (2014).
- Zhang, H. *et al.* Topological insulators in Bi_2Se_3 , Bi_2Te_3 and Sb_2Te_3 with a single Dirac cone on the surface. *Nat. Phys* **5**, 438–442 (2009).
- Qi, X.-L. & Zhang, S.-C. Topological insulators and superconductors. *Rev. Mod. Phys.* **83**, 1057–1110 (2011).
- Moore, J. E. The birth of topological insulators. *Nature* **464**, 194–198 (2010).
- McIver, J. W., Hsieh, D., Steinberg, H., Jarillo-Herrero, P. & Gedik, N. Control over topological insulator photocurrents with light polarization. *Nat. Nanotechnol* **7**, 96–100 (2012).

- Duan, J. *et al.* Identification of helicity-dependent photocurrents from topological surface states in Bi_2Se_3 gated by ionic liquid. *Sci. Rep* **4**, 4889 (2014).
- Olbrich, P. *et al.* Room-temperature high-frequency transport of Dirac fermions in epitaxially grown Sb_2Te_3 - and Bi_2Te_3 -based topological insulators. *Phys. Rev. Lett.* **113**, 096601 (2014).
- Luo, C. W. *et al.* THz generation and detection on Dirac fermions in topological insulators. *Adv. Opt. Mater.* **1**, 804–808 (2013).
- Zhu, L.-G., Kubera, B., Fai Mak, K. & Shan, J. Effect of surface states on terahertz emission from the Bi_2Se_3 surface. *Sci. Rep* **5**, 10308 (2015).
- Tu, C.-M. *et al.* Manifestation of a second Dirac surface state and bulk bands in THz radiation from topological insulators. *Sci. Rep* **5**, 14128 (2015).
- Bas, D. A. *et al.* Coherent control of injection currents in high-quality films of Bi_2Se_3 . *Appl. Phys. Lett.* **106**, 041109 (2015).
- Kastl, C., Karmetzky, C., Karl, H. & Holleitner, A. W. Ultrafast helicity control of surface currents in topological insulators with near-unity fidelity. *Nat. Commun* **6**, 6617 (2015).
- Leitenstorfer, A., Hunsche, S., Shah, J., Nuss, M. & Knox, W. Detectors and sources for ultrabroadband electro-optic sampling: experiment and theory. *Appl. Phys. Lett.* **74**, 1516–1518 (1999).
- Leitenstorfer, A., Hunsche, S., Shah, J., Nuss, M. C. & Knox, W. H. Femtosecond charge transport in polar semiconductors. *Phys. Rev. Lett.* **82**, 5140–5143 (1999).
- Kampfrath, T. *et al.* Terahertz spin current pulses controlled by magnetic heterostructures. *Nat. Nanotechnol* **8**, 256–260 (2013).
- Liu, C.-X. *et al.* Model hamiltonian for topological insulators. *Phys. Rev. B* **82**, 045122 (2010).
- Zhang, W., Yu, R., Zhang, H.-J., Dai, X. & Fang, Z. First-principles studies of the three-dimensional strong topological insulators Bi_2Te_3 , Bi_2Se_3 and Sb_2Te_3 . *New J. Phys.* **12**, 065013 (2010).
- Roy, S. *et al.* Atomic relaxations at the (0001) surface of Bi_2Se_3 single crystals and ultrathin films. *Phys. Rev. B* **90**, 155456 (2014).
- McIver, J. W. *et al.* Theoretical and experimental study of second harmonic generation from the surface of the topological insulator Bi_2Se_3 . *Phys. Rev. B* **86**, 035327 (2012).
- Park, K., Beule, C. D. & Partoens, B. The ageing effect in topological insulators: evolution of the surface electronic structure of Bi_2Se_3 upon K adsorption. *New J. Phys.* **15**, 113031 (2013).
- Nastos, F. & Sipe, J. E. Optical rectification and current injection in unbiased semiconductors. *Phys. Rev. B* **82**, 235204 (2010).
- Lewis, R. A. A review of terahertz sources. *J. Phys. D Appl. Phys* **47**, 374001 (2014).
- Hosur, P. Circular photogalvanic effect on topological insulator surfaces: Berry-curvature-dependent response. *Phys. Rev. B* **83**, 035309 (2011).
- Ganichev, S. D. *et al.* Resonant inversion of the circular photogalvanic effect in n-doped quantum wells. *Phys. Rev. B* **68**, 035319 (2003).
- Schmidt, C. B., Priyadarshi, S., Tarasenko, S. A. & Bieler, M. Ultrafast magneto-photocurrents in GaAs: separation of surface and bulk contributions. *Appl. Phys. Lett.* **106**, 142108 (2015).
- Priyadarshi, S., Pierz, K. & Bieler, M. All-optically induced ultrafast photocurrents: beyond the instantaneous coherent response. *Phys. Rev. Lett.* **109**, 216601 (2012).
- Sobota, J. *et al.* Ultrafast electron dynamics in the topological insulator Bi_2Se_3 studied by time-resolved photoemission spectroscopy. *J. Electron. Spectrosc. Relat. Phenom* **195**, 249–257 (2014).
- Boschini, F. *et al.* Coherent ultrafast spin-dynamics probed in three dimensional topological insulators. *Sci. Rep* **5**, 15304 (2015).
- Weber, W. *et al.* Quantum ratchet effects induced by terahertz radiation in GaN-based two-dimensional structures. *Phys. Rev. B* **77**, 245304 (2008).
- Glass, A. M., von der Linde, D. & Negran, T. J. High-voltage bulk photovoltaic effect and the photorefractive process in LiNbO_3 . *Appl. Phys. Lett.* **25**, 233–235 (1974).
- Johnston, M. B., Whittaker, D. M., Corchia, A., Davies, A. G. & Linfield, E. H. Simulation of terahertz generation at semiconductor surfaces. *Phys. Rev. B* **65**, 165301 (2002).
- Malevich, V. L., Adomavičius, R. & Krotkus, A. THz emission from semiconductor surfaces. *C. R. Phys.* **9**, 130–141 (2008).
- Shan, J. & Heinz, T. F. in *Ultrafast Dynamical Processes in Semiconductors* vol. 92, 1–56 (Topics in Applied Physics, 2004).
- Sipe, J. E. & Shkrebti, A. I. Second-order optical response in semiconductors. *Phys. Rev. B* **61**, 5337–5352 (2000).
- Laman, N., Bieler, M. & Van Driel, H. Ultrafast shift and injection currents observed in wurtzite semiconductors via emitted terahertz radiation. *J. Appl. Phys.* **98**, 103507–103507 (2005).
- Apostolopoulos, V. & Barnes, M. THz emitters based on the photo-Dember effect. *J. Phys. D Appl. Phys* **47**, 374002 (2014).
- Nastos, F. & Sipe, J. E. Optical rectification and shift currents in GaAs and GaP response: below and above the band gap. *Phys. Rev. B* **74**, 035201 (2006).

39. Côté, D., Laman, N. & Van Driel, H. Rectification and shift currents in GaAs. *Appl. Phys. Lett.* **80**, 905–907 (2002).
40. Ferguson, B. & Zhang, X.-C. Materials for terahertz science and technology. *Nat. Mater.* **1**, 26–33 (2002).
41. Shen, Y.-R. *Principles of Nonlinear Optics* (Wiley-Interscience, 1984).
42. Madelung, O., Rössler, U. & Schulz, M. in *Non-Tetrahedrally Bonded Elements and Binary Compounds I* 1–3 (Landolt-Börnstein - Group III Condensed Matter, Springer, 1998).
43. Gnezdilov, V. *et al.* Helical fluctuations in the Raman response of the topological insulator Bi₂Se₃. *Phys. Rev. B* **84**, 195118 (2011).
44. Plank, H. *et al.* Photon drag effect in (Bi_{1-x}Sb_x)₂Te₃ three-dimensional topological insulators. *Phys. Rev. B* **93**, 125434 (2016).
45. Cabellos, J. L., Mendoza, B. S. & Shkrebtii, A. I. Optical coherent current control at surfaces: theory of injection current. *Phys. Rev. B* **84**, 195326 (2011).
46. Krumrain, J. *et al.* MBE growth optimization of topological insulator Bi₂Te₃ films. *J. Cryst. Growth* **324**, 115–118 (2011).
47. Mishra, S. K., Satpathy, S. & Jepsen, O. Electronic structure and thermoelectric properties of bismuth telluride and bismuth selenide. *J. Phys. Condens. Matter* **9**, 461 (1997).
48. Roushan, P. *et al.* Topological surface states protected from backscattering by chiral spin texture. *Nature* **460**, 1106–1109 (2009).
49. Wang, M., Qiao, S., Jiang, Z., Luo, S. & Qi, J. Unraveling photoinduced spin dynamics in the topological insulator Bi₂Se₃. *Phys. Rev. Lett.* **116**, 036601 (2016).
50. Valdés Aguilar, R. *et al.* Terahertz response and colossal Kerr rotation from the surface states of the topological insulator Bi₂Se₃. *Phys. Rev. Lett.* **108**, 087403 (2012).
51. Bansal, N., Kim, Y. S., Brahlek, M., Edrey, E. & Oh, S. Thickness-independent transport channels in topological insulator Bi₂Se₃ thin films. *Phys. Rev. Lett.* **109**, 116804 (2012).
52. Zhang, P. & Wu, M. W. Hot-carrier transport and spin relaxation on the surface of topological insulator. *Phys. Rev. B* **87**, 085319 (2013).
53. Junck, A., Refael, G. & von Oppen, F. Photocurrent response of topological insulator surface states. *Phys. Rev. B* **88**, 075144 (2013).
54. Kuroda, K., Reimann, J., Gütde, J. & Höfer, U. Generation of transient photocurrents in the topological surface state of Sb₂Te₃ by direct optical excitation with midinfrared pulses. *Phys. Rev. Lett.* **116**, 076801 (2016).
55. Sánchez-Barriga, J. *et al.* Photoemission of Bi₂Se₃ with circularly polarized light: probe of spin polarization or means for spin manipulation? *Phys. Rev. X* **4**, 011046 (2014).
56. Liu, Q., Zhang, X., Abdalla, L., Fazzio, A. & Zunger, A. Switching a normal insulator into a topological insulator via electric field with application to phosphorene. *Nano Lett.* **15**, 1222–1228 (2015).
57. Xia, Y. *et al.* Observation of a large-gap topological-insulator class with a single Dirac cone on the surface. *Nat. Phys* **5**, 398–402 (2009).
58. Hruban, A. *et al.* Influence of chemical composition of liquid phase and growth process on physical properties of Bi₂Se₃, Bi₂Te₃ and Bi₂Te₂Se compounds. *Acta Phys. Pol. A* **120**, 950–953 (2011).
59. Mills, D. L. *Nonlinear Optics: Basic Concepts* (Springer Science & Business Media, 2012).

Acknowledgements

We thank S.D. Ganichev, A.D. Bristow and N.P. Armitage for stimulating and fruitful discussions. We are grateful to the German Science Foundation (DFG) for financial support through priority program SPP 1666 ‘Topological insulators: materials, fundamental properties, devices’ (grant no. KA 3305/3 and MU 1780/10). T.K. acknowledges the European Research Council for support through grant no. 681917 (TERAMAG). L.P. and M.K. thank for the support by grant ANR-13-IS04-0001-01.

Author contributions

T.K. and L.B. conceived the experiments. G.M. and A.H. grew samples. L.B. performed the terahertz experiments and analysed the experimental data with contributions from T.K. L.P. and M.K. characterized samples by ARPES and transport measurements. T.K., L.B., M.W., M.M. and L.P. co-wrote the paper. All the authors contributed to discussing the results and writing the paper.

Additional information

Supplementary Information accompanies this paper at <http://www.nature.com/naturecommunications>

Competing financial interests: The authors declare no competing financial interests.

Reprints and permission information is available online at <http://npg.nature.com/reprintsandpermissions/>

How to cite this article: Braun, L. *et al.* Ultrafast photocurrents at the surface of the three-dimensional topological insulator Bi₂Se₃. *Nat. Commun.* **7**, 13259 doi: 10.1038/ncomms13259 (2016).

Publisher's note: Springer Nature remains neutral with regard to jurisdictional claims in published maps and institutional affiliations.



This work is licensed under a Creative Commons Attribution 4.0 International License. The images or other third party material in this article are included in the article's Creative Commons license, unless indicated otherwise in the credit line; if the material is not included under the Creative Commons license, users will need to obtain permission from the license holder to reproduce the material. To view a copy of this license, visit <http://creativecommons.org/licenses/by/4.0/>

© The Author(s) 2016